RAD51 regulates eukaryotic chromatin motions in the absence of DNA damage

Amine Maarouf¹, Fadil Igbal², Sarvath Sanaullah³, Maëlle Locatelli⁴, Andrew T. Atanasiu⁴,

Daniel Kolbin⁴, Chloé Hommais¹, Joëlle Mühlemann⁵, Keith Bonin⁶, Kerry Bloom⁴, Jing Liu⁷,

Pierre-Alexandre Vidi^{1,3,#}

¹ Institut de Cancérologie de l'Ouest, F-49055 Angers, France

² Department of Physics, Indiana University-Purdue University Indianapolis, Indianapolis, IN 46202, USA

³ Department of Cancer Biology, Wake Forest School of Medicine, Winston-Salem, NC 27157, USA

⁴ Department of Biology, University of North Carolina at Chapel Hill, Chapel Hill, NC 27599, USA

⁵ Climate Resilient Crop Production Laboratory, Division of Crop Biotechnics, Department of Biosystems, Katholieke

Universiteit (KU) Leuven, Leuven, 3000, Belgium

⁶ Department of Physics, Wake Forest University, Winston-Salem, NC 27109, USA

⁷ Department of Physics and Astronomy, Purdue University, West Lafayette, IN 47907, USA

To whom correspondence should be addressed: pierre.vidi@ico.unicancer.fr

Keywords: RAD51, chromatin mobility, mammalian cells, yeasts, plants.

Running Head: RAD51 and chromatin motions

1

ABSTRACT

In yeasts and higher eukaryotes, chromatin motions may be tuned to genomic functions, with transcriptional activation and the DNA damage response both leading to profound changes in chromatin dynamics. The RAD51 recombinase is a key mediator of chromatin mobility following DNA damage. As functions of RAD51 beyond DNA repair are being discovered, we asked if RAD51 modulates chromatin dynamics in the absence of DNA damage and found that inhibition or depletion of RAD51 alters chromatin motions in undamaged cells. Inhibition of RAD51 increased nucleosome clustering. Predictions from polymer models are that chromatin clusters reduce chain mobility and, indeed, we measured reduced motion of individual chromatin loci in cells treated with a RAD51 inhibitor. This effect was conserved in mammalian cells, yeasts, and plant cells. In contrast, RAD51 depletion or inhibition increased global chromatin motions at the microscale. The results uncover a role for RAD51 in regulating local and global chromatin dynamics independently from DNA damage and highlight the importance of considering different physical scales when studying chromatin dynamics.

Significance statement

- Chromatin motions are influenced by and may regulate genomic processes.
- The RAD51 recombinase, a key factor in homologous recombination repair of DNA double-strand breaks, modulates chromatin dynamics, even in the absence of DNA damage. This effect is conserved in mammalian cells, yeasts, and plant cells.
- The results expand the growing number of non-canonical (DNA repair-independent) roles of RAD51 and provide a new approach to manipulate chromatin dynamics.

INTRODUCTION

Genomic functions including replication, transcription, and repair have an influence on (and may be regulated by) chromatin motions. DNA damage profoundly affects chromatin dynamics (Seeber *et al.*, 2018; Lawrimore *et al.*, 2020; Mine-Hattab and Chiolo, 2020). In yeast, DNA double-strand breaks (DSBs) induced by genotoxic drugs or restriction enzymes lead to increased motion of the chromatin chain flanking the break, as well as globally on other chromosomes (Mine-Hattab and Rothstein, 2012; Neumann *et al.*, 2012; Dion *et al.*, 2013; Seeber *et al.*, 2013; Herbert *et al.*, 2017; Lawrimore *et al.*, 2017). Increased mobility facilitates homology search and strand invasion during homologous recombination repair (HRR) (Mine-Hattab and Rothstein, 2012; Challa *et al.*, 2021; Garcia Fernandez *et al.*, 2022). The impact of DSBs on chromatin dynamics in higher eukaryotes is more nuanced and less understood. DNA repair foci are more mobile than other nuclear hallmarks (Krawczyk *et al.*, 2012) and dysfunctional telomeres (resembling DSBs) diffuse faster than capped, functional telomeres (Dimitrova *et al.*, 2008). Yet, measurements in undamaged nuclear regions have revealed decreased global chromatin motions in response to damage, with higher mobility retained at or near break sites (Liu *et al.*, 2015; Locatelli *et al.*, 2022).

The RAD51 (RADiation sensitive protein 51) recombinase is a key HRR factor. The protein forms helical nucleoprotein filaments on resected ssDNA and is involved in homology search and pairing with the homologous sequence. The local increase in yeast chromatin motions following DNA damage depends on the RAD51 homolog (scRad51) (Mine-Hattab and Rothstein, 2012; Smith et al., 2018; Smith et al., 2019; Garcia Fernandez et al., 2022). This effect, proximal to the break sites, may be explained, at least in part, by stiffening and increased persistence length of chromatin after the formation of Rad51 nucleofilaments (Mine-Hattab et al., 2017). ScRad51 also plays a context-dependent role in global chromatin mobility after DNA damage (Garcia Fernandez and Fabre, 2022). Specifically, scRad51 is necessary for radiation induced mobility of distal, undamaged loci in diploid cells (Mine-Hattab and Rothstein, 2012; Smith et al., 2018). Whereas scRad51 is generally excluded from stalled replication forks until their relocation to the 'safe haven' of the nuclear periphery (Su et al., 2015), peripheral relocation of replication forks arrested by replication fork barriers occurs after scRad51 loading (Kramarz et al., 2020), implicating the protein in directed chromatin motions in the absence of DNA damage. ScRad51 may also participate in the formation of damage-induced nuclear microtubule filaments which mediate DNA break translocation to the periphery of yeast nuclei (Oshidari et al., 2018). Less is known about the contribution of RAD51 to chromatin dynamics in higher eukaryotes. In mammalian cancer cells relying on the alternative lengthening of telomeres (ALT) pathway to maintain their

telomeres, damaged telomeres undergo directed motions which depend on RAD51 for homology-directed synthesis of telomeric DNA (Cho *et al.*, 2014). These findings suggest that RAD51 may be an important chromatin mobility factor across species.

Non-canonical roles of yeast and mammalian RAD51 have been described, some of which are independent of the well-known HRR functions of the protein. RAD51 promotes the formation of R-loops of DNA-RNA hybrids (Wahba *et al.*, 2013; Feretzaki *et al.*, 2020; Girasol *et al.*, 2023). While R-loops can lead to genomic instability, they also play physiological roles in transcription activation and termination (Crossley *et al.*, 2019; Niehrs and Luke, 2020). Importantly, accumulation of scRad51 at R-loops occurs before the formation of DNA breaks at these structures (Wahba *et al.*, 2013). In the context of DNA replication stress, RAD51 nucleofilaments protect stalled replication forks, independently from the recombination function of the protein, by promoting fork reversal (Wassing and Esashi, 2021). Considering these HRR-independent functions of RAD51 and the role of the protein in chromatin mobility following DNA damage, we asked if the protein regulates chromatin dynamics in undamaged cells. We find that RAD51 depletion or a short pharmacological inhibition of RAD51 alters chromatin dynamics, and that this effect is dependent on the physical scale considered.

RESULTS

RAD51 modulates mammalian chromatin microdomains motions

RAD51 is a key influencer of chromatin mobility in response to DNA damage (Mine-Hattab and Rothstein, 2012; Cho *et al.*, 2014; Smith *et al.*, 2018; Smith *et al.*, 2019; Garcia Fernandez *et al.*, 2022). Since a growing number of functions independent from DNA repair are being discovered for the protein, we set out to determine if RAD51 affects chromatin dynamics in the absence of DNA damage. We recently developed a method based on structured illumination to map the motions of chromatin microdomains in mammalian cells (Bonin *et al.*, 2018; Locatelli *et al.*, 2022). The method relies on a diffractive optical element producing an array of beamlets that activate photoactivatable GFP fused to histone H2A in the nucleus of cells (PAGFP-H2A; Fig. 1A), which results in a 7 x 7 lattice of fluorescent spots. The measurements reflect diffusion (*D*) of chromatin microdomains.

To determine if RAD51 modulates mammalian chromatin motions, we generated a U2OS cell line with reduced RAD51 levels by stably expressing Cas9 and a *RAD51*-specific guide RNA. We achieved a ~60% reduction in *RAD51* expression, but not complete depletion, as determined by

western blot and immunostaining (Fig. 1B-C). This was expected since *RAD51* is an essential gene in mammalian cells (Tsuzuki *et al.*, 1996). RAD51 KD cells had increased sensitivity to mitomycin C, a DNA cross-linker inducing DNA breaks predominantly repaired by homologous recombination (Suppl. Fig. S1). These results confirmed reduced RAD51 function in the knockdown cell line.

Chromatin microdomains were significantly more mobile in RAD51 KD cells compared to the parental cell line (Fig. 1D). To further assess the influence of RAD51 on chromatin motions, we used the B02 (Huang *et al.*, 2011; Huang *et al.*, 2012) and RI-1 (Budke *et al.*, 2012) inhibitors, which prevent the interaction of the protein with single-stranded DNA and filament formation. As expected, these treatments prevented the formation of RAD51 repair foci in cells with DNA damage (Suppl. Fig. S2). B02 and RI-1 treatments significantly increased chromatin microdomain motions, (Fig. 1E), suggesting that RAD51 limits chromatin motions at the microscale.

Increased chromatin microdomain mobility upon RAD51 inhibition is independent from DNA damage

RAD51 is a key factor for DNA double-strand break repair by HRR. Accordingly, prolonged inhibition of RAD51 is expected to increase the DNA damage burden, complicating data interpretation. We and others have indeed shown a complex effect of DNA damage on chromatin dynamics (Seeber et al., 2018; Locatelli et al., 2022). We therefore identified treatment conditions with the B02 RAD51 inhibitor, namely a dose of 10 µm applied for 1h, which did not lead to reduced cell viability (Fig. 2A), nor to the induction of DNA breaks, quantified by neutral comet assays (Fig. 2B), by immunostaining for YH2AX (Fig. 2C), and visualized with mCherry fused to the c-terminus of 53BP1 (Dimitrova et al., 2008) (Fig. 2D). With these conditions (10 µM B02 for 1h), acceleration of chromatin microdomain motion was conserved (Fig. 2E), despite the absence of DNA damage induction. Within a population, U2OS cells have varying levels of endogenous DNA breaks. We therefore also guided chromatin mobility analyses to cells with no or very few DNA damage foci and still observed B02's effect on chromatin mobility (Fig. 2F). Finally, HRR is predominantly active in S and G2 phases of the cell cycle when sister chromatids are available for recombination repair. In experiments with enriched G1 cell populations, we measured the same B02-induced increased chromatin microdomain motions, suggesting that this effect is cell eycle-independent, or at least not restricted to S/G2-phases (Fig. 2G). As expected, the short (1h) exposure to B02 did not alter cell cycle distribution (Suppl. Fig. S3), ruling out potential effects associated with proliferation. We found previously that manipulation of chromatin compaction with histone deacetylase or demethylase inhibitors alters chromatin microdomain motions (Locatelli et al., 2022). However, in our short treatment conditions, no appreciable change in methylated nor acetylated histone H3 (H3K9me3 and -ac) was detected (Suppl. Fig. S4). Collectively, the results suggest that inhibition of RAD51 affects chromatin mobility independently from RAD51's function in DNA repair.

RAD51 inhibition increases nucleosome clustering

To measure the effect of RAD51 inhibition on the dynamics and nanoscale organization of single nucleosomes, we used a single molecule imaging approach with cells expressing histone H2B fused to the HaloTag, labeled with a fluorescent HaloTag ligand (Kefer *et al.*, 2021) (Fig. 3A). First, we tracked single nucleosomes in time-lapse movies from cells with sparsely labeled H2B. As shown in Fig. 3B, there was no significant difference in nucleosome diffusion speed in cells treated with B02 compared to controls. Therefore, our results show different dependencies for chromatin motions at different physical scales.

Next, we analyzed nanoscale chromatin organization with super-resolution imaging, using direct STochastic Optical Reconstruction Microscopy (dSTORM) (Van de Linde *et al.*, 2011). We used the same H2B-HT cell system, but with dense labeling of nucleosomes with the HaloTag ligand (Fig. 3C and Suppl. Fig. S5A). Qualitatively, nucleosomes were more dispersed in the control than in cells treated with B02, although the number of nucleosomes detected in the reconstituted dSTORM images were similar in both conditions. Quantification of spatial dependencies using Besag's L-function (Fig. 3D and Suppl. Fig. S5A-B) confirmed a clustered distribution of nucleosomes at the 100 nm distance band (Bancaud *et al.*, 2009; Ricci *et al.*, 2015; Nozaki *et al.*, 2017; Miron *et al.*, 2020). In cells treated with B02, the L-function had a higher peak, shifted to the left (Fig. 3E), interpreted as increased nucleosome clustering and smaller cluster sizes. An alternative explanation would be that B02 massively decreases histone contents. This was however not seen by western blot (Suppl. Fig. S4A). Moreover, quantification from dSTORM images revealed no difference in the total number of H2B-HT molecules between controls and RAD51-inhibited cells (Suppl. Fig. S5C). Hence, there was rearrangement rather than loss of nucleosomes in B02-treated cells.

Nanoscale clusters lower the mobility of chromatin loci in a biophysical chromatin model To predict the effect of nucleosome clustering on the mobility of chromatin loci, we used a beadand-spring polymer model with different levels of looping (crosslinks) to simulate clusters. Crosslinks within or between chains in the model represent chromatin interactions with proteins such as condensin or cohesin. Introduction of crosslinking within or between polymer chains

recapitulates key experimental observations of nucleoli in budding yeast (Hult *et al.*, 2017; Walker *et al.*, 2019). For example, changes in crosslinking account for the heterogeneity in the density of ribosomal DNA within the nucleolus, the crescent shape of the nucleolus, and the position of two chains in cells with the ribosomal DNA split between two chromosomes (Hult *et al.*, 2017). To determine the consequences of nucleosome clustering on chromatin mobility we examined chromatin motion in the absence or presence of crosslinking (Fig. 4A). The crosslinks are dynamic through regulation of the mean On and Off times of binding. Two crosslinking regimes were implemented: fast crosslinking (0.19 s On / 0.019s Off), which results in rigid chromatin clusters, and slow crosslinking (10 s On / 1 s Off), resulting in more flexible clusters. Our model predicts a decrease in chromatin mobility in the presence of either rigid or flexible clusters compared to unconstrained chains (no looping) (Fig. 4B).

RAD51 inhibition reduces motions of individual chromatin loci

To assess B02's effect on the dynamics of individual chromatin loci, matching the physical scale represented by our biophysical model, we expressed the Lac-repressor fused to GFP and a nuclear localization signal (Lacl-GFP) in U2OS cells with a stable genomic integration of *lacO* arrays (Vidi *et al.*, 2012) (Fig. 5A). As expected, Lacl-GFP diffusion values measured in live cells were more than an order of magnitude higher than in fixed cells, indicating a negligible contribution of noise and drift to the chromatin diffusion measurements (Fig. 5B). Using the same B02 treatment condition as for the chromatin microdomain and single nucleosome analyses (1h, 10 μM), we found that the drug significantly decreased Lacl-GFP motions (Fig. 5B), as predicted *in silico*.

RAD51 is a highly conserved protein. Human RAD51 notably shares 67% with yeast scRad51 and 69% identity with the *Arabidopsis thaliana* RAD51 ortholog (AtRAD51). Molecular docking studies indicate that B02 binds within the RAD51 dimerization interface and/or RAD51's Walker ATP binding site of RAD51 (Vydyam *et al.*, 2019; Shkundina *et al.*, 2021). Both domains are conserved across species (Suppl. Fig. S6). To determine if the effect of RAD51 inhibition on chromatin loci motions is a general phenomenon, we used other model organism in which Lac array systems have been developed to track chromatin motions: budding yeast and the plant *Arabidopsis thaliana*. As in mammalian cells, we measured slower chromatin loci motions after B02 treatment in yeasts (Fig. 5C-D). In *S. cerevisiae*, DSBs cause the accumulation of Rad52 into prominent repair foci (Lisby *et al.*, 2001; Lawrimore *et al.*, 2017). Using cells expressing Rad52-GFP, we found that, as in mammalian cells, the B02 treatment did not cause DNA breaks, nor prevent the DNA damage response elicited by bleomycin treatment (Suppl. Fig. S7A-B). The

effect of B02 therefore appears to be unrelated to HRR functions of scRad51. At a higher concentration (100 μ M), B02 did block Rad52 foci formation following bleomycin treatment, indicating that the inhibitor is also active against scRad51 (Suppl. Fig. S7C).

Next, we tested the effect of B02 on plant chromatin motions, using lacO/LacI-GFP Arabidopsis thaliana lines (Meschichi et al., 2022). We focused on primary root tips, which have clear LacI-GFP signals (Fig. 5E). To assess the effect of RAD51 inhibition on chromatin motions in this system, seedlings were transferred onto B02-containing growth substrate (or growth substrate without B02 as control) and imaged 16-18h later. We extended the treatment time (compared to mammalian cells and yeasts) to ensure penetration of the molecule throughout the root tissue. The diffusion speed of individual LacI-GFP foci was reduced in roots treated with B02 (Suppl. Fig. S8). In the division zone, the vast majority of cell nuclei have two fluorescent LacI-GFP spots. We could therefore use paired particle tracking to assess B02's effect on chromatin motions. With this approach, fluctuation of the distance between the fluorescent spot is measured as a function of time (Liu et al., 2015) (Fig. 5F). Comparing the average change in spot separation between frames (Fig. 5G) further indicates that the effect of B02 on chromatin dynamics (at least at the level of individual chromatin loci) is conserved in plant cells. We made the same observation in two independent Arabidopsis IacO/LacI-GFP lines. In conclusion, using the same molecular tool in different species, we find that the effect of RAD51 inhibition on chromatin loci dynamics is conserved.

DISCUSSION

Our results show that inhibition of RAD51 alters chromatin dynamics, in the absence of DNA damage, and that this effect is dependent on the physical scale considered. Previous work revealed that nuclear processes influence chromatin motions differentially at different scales. For example, the cell cycle status influences motions of individual chromatin loci (1-2 kb) but not of single nucleosomes or chromatin microdomains (Heun *et al.*, 2001; Ma *et al.*, 2019; lida *et al.*, 2022; Locatelli *et al.*, 2022). Also, the transcription machinery 'stirs' actively transcribed regions, and motions of enhancers and promoters increase upon activation (Gu *et al.*, 2018). Yet, globally, active RNA polymerase II constrains nucleosome motions, likely by stabilizing chromatin domains around transcription hubs (Nagashima *et al.*, 2019). Chromatin motion regimes are distinct at different physical scales, and we indeed find that RAD51 inhibition has an impact on chromatin

motions at the microscale, without affecting single nucleosome motions. At the nanoscale, thermal effects are likely major contributors to the molecular dynamics.

At the scale of chromatin microdomains, RAD51 inhibition or depletion leads to a global increase in chromatin dynamics. A possible explanation is that nucleic acid structures stabilized by RAD51 (such as R-loops) may be inherently less mobile or less prone to collective microscale motions. For example, R-loops regulate DNA loop extrusion by cohesin (Zhang *et al.*, 2023), a key driver of chromatin dynamics. Interestingly, a scRad51 mutant defective in strand exchange (and hence HRR) but able to bind ssDNA retains the capacity to increase diffusion of chromatin loci distal from DNA breaks, indicating that ssDNA binding is an important regulator of global chromatin mobility (Smith *et al.*, 2018). We note that $rad51\Delta$ yeast strains have similar chromatin dynamics compared to wild-type cells in the absence of DNA damage (Seeber *et al.*, 2013; Smith *et al.*, 2018), suggesting that in yeast, depleting vs inhibiting Rad51 leads to different outcomes.

It is also important to consider that RAD51 binds dsDNA (Benson *et al.*, 1994; Zaitseva *et al.*, 1999) and that B02 may inhibit dsDNA binding by RAD51 (Huang *et al.*, 2012). In contrast to ssDNA binding necessary for the recombination process, dsDNA binding by RAD51 protects DNA and inhibits pairing with homologous sequences (Zaitseva *et al.*, 1999). The non-canonical function of RAD51 in the protection of reversed replication forks (distinct from its recombination function) relies on dsDNA binding (Halder *et al.*, 2022). It remains to be established if RAD51 binds dsDNA in other contexts, which may globally affect chromatin dynamics. RAD51 ChIPseq data do indicate an enrichment of the protein at active chromatin regions (which are preferentially repaired by HRR), where it co-localizes with transcription factors (Aymard *et al.*, 2014; Hazan *et al.*, 2019). A re-analysis of these datasets indicates preferential binding of RAD51 to enhancer box elements (Kang *et al.*, 2021), suggesting a role of RAD51 in transcription regulation, with the caveat that it is difficult to control for the presence/absence of DNA breaks in cell population-based assays.

Homology between RAD51 orthologs in eukaryotes is high. Moreover, B02 inhibits RAD51 foci formation and HRR both in human cells (Huang *et al.*, 2012; Urban *et al.*, 2016) and in *Plasmodium falciparum* (Vydyam *et al.*, 2019), indicating that B02's inhibitory mechanism is conserved across species. It was therefore not surprising to measure similar effects of the B02 RAD51 inhibitor in mammalian cells, yeasts, and plants. As in mammalian cells, the effect in yeasts was very likely independent from scRad51's role in HRR since B02 did not cause DNA damage in yeast cells. As documented in yeast, DNA damage in plants increases the mobility of *LacO* chromatin arrays (Meschichi *et al.*, 2022). Yet (and in contrast to the increased motions of

chromatin microdomains), B02 reduced mobility of *lacO* genomic loci across species, further arguing for an effect independent from the canonical role of RAD51 in HRR. Based on superresolution imaging, the drug also increases chromatin nanodomain clustering, predicted by our model to reduce mobility at the 5 kb scale (5 kb DNA/spring). Future work is needed to determine how RAD51 inhibition affects nanoscale chromatin organization.

MATERIALS AND METHODS

Mammalian cell culture and treatments

U2OS osteosarcoma cells were cultured in DMEM supplemented with 10% fetal bovine serum (Sigma) in a humidified incubator at 37°C, 5% CO₂. Cultures were tested routinely for mycoplasma contamination; all tests were negative. Knock down of RAD51 was achieved by transducing cells with lentiviral particles combining Cas9 and sgRNA under the hEF1a promoter (Horizon discovery, Edit-R All-in-one lentiviral system [lentiviral particles; 10⁷ TU/ml], cat# VSGH11936-247505860). The target sequence was TTGGCCCACAACCCATTTCA, corresponding to exon 2 of RAD51 (genomic location: chr15:40698817-40698839). A 1:50 dilution of the lentiviral particles was used for transduction. Transduced cells were selected with puromycin (2 µg/ml). For imaging, cells were seeded in 35 mm glass-bottom dishes (MatTek) at 100,000 cells per dish. For fixation, cells were incubated 20 min in 4% paraformaldehyde (Sigma # HT5011; 20 min). Treatments with B02 (3-(Phenylmethyl)-2-[(1E)-2-(3-pyridinyl)ethenyl]-4(3H)-quinazolinone; Cat# SML0364) were for one hour, at the concentrations indicated in the Results section. RI-1 (GlpBio, Cat# GC18140) was diluted to 25 µM and added to the cells for 24h. Bleomycin (Cayman Chemical; 20 mU/ml, 2h) or mitomycin C (Accord; 2.5 µM, 18h) was applied to the cells for 1h to induce DNA damage. The double thymidine block was used for cell cycle synchronization as described (Harper, 2005).

Tracking chromatin microdomains in mammalian cells

Photoactivated lattices of chromatin microdomains were generated in U2OS PAGFP-H2A cells (Locatelli *et al.*, 2022) with a custom diffractive optical element module inserted into the condenser arm of an inverted Olympus IX83 microscope (Bonin *et al.*, 2018). Cells were kept at 37°C in the custom-built enclosure of the microscope. Images were taken with a 60x oil lens (N.A. = 1.35) and an sCMOS camera (Hamamatsu ORCA-Flash 4.0), using the CellSens software. Movies were recorded over one minute at 3.3 frames per second (fps). The image sequences were registered using the StackReg plugin in FIJI (Thevenaz *et al.*, 1998). Tracking of chromatin

microdomains was done in MATLAB, as described (Bonin *et al.*, 2018; Locatelli *et al.*, 2022). To avoid potential confounding effects of large nuclear deformation, cells with distortions greater than an arbitrary threshold ($\Delta L \ge 400$ pixels, with ΔL , the cumulative change in the perimeter of the largest quadrilateral defined by the grid of spots, see below) were excluded from the analyses.

Tracking genomic loci in mammalian cells

U2OS cells with a stable genomic integration of Lac repressor binding arrays (*lacO*; 256 copies; (Vidi *et al.*, 2012)) were used to measure the mobility of genomic loci. LacI-GFP was transiently expressed using Lipofectamine 3000 (Invitrogen)-mediated transfection, performed 48h before imaging. Image sequences were collected with an IX83 Olympus microscope equipped with an ORCA-Quest qCMOS camera (Hamamatsu) and a 40x air objective (N.A. = 0.95). A TokaiHit stage incubator was used to maintain environmental conditions (37°C, 5% C0₂). Excitation light was from the 475 nm line of a LED illumination system (X-Cite TURBO, Excelitas). Emitted light was filtered using a 525/50 nm filter (Chroma). The frame rate was 3 fps. For analysis, individual cells were cropped from the time-lapses and registered with StackReg (rigid body translations/rotations) (Thevenaz *et al.*, 1998). The MOSAIC Particle Tracker (Sbalzarini and Koumoutsakos, 2005) was used to detect LacI-GFP spots, track trajectories, and compute chromatin diffusion from mean-squared displacement (MSD) plots. Some diffusion values were aberrant (supra-physiological), likely due to tracking errors, and were excluded using an outlier analysis (ROUT method, Q = 0.1).

Tracking genomic loci in yeasts

Budding yeast strain KS406 (MATalpha, ade5-1, trp1-289, ura3del, leu2-3, 112, lys2::insl-Sce1 [lacO array next to RAD16 promoter, tetO array next to LYS2 promoter (pRS305tetO)], arg4::hisG Gal1/10 I-Sce1, thr1::HISpLacI-GFP:Nat, ade1::URAptetR-CFP:Hyg, Spc29-RFP:Bsd) and KBY3584 (YEF 473A Rad52-GFP::Kan Spc29-CFP::HygB) were grown to mid-log phase at 24°C in liquid YEPD and imaged in YC complete medium with 2% filter-sterilized glucose added. Image sequences were acquired on an Eclipse Ti wide-field inverted microscope (Nikon) with a 100x Apo TIRF 1.49 NA objective (Nikon) and a Clara charge-coupled device camera (Andor) using the Nikon NIS Elements imaging software. Images were taken over 20 minutes with 30 seconds intervals. Each interval contained a seven-step Z-stack of 400-nm step size, acquired for KS406 in the GFP (lacO array), RFP (SPB) and Trans channels, or for KBY3584 in the GFP (Rad52), CFP (SPB) and transmission channels. After manual cropping, time lapses were tracked using TrackMate (FIJI plugin) and a custom MATLAB program to compute MSD, or Rad52 positive cells counted.

Tracking genomic loci in plant cells

The Arabidopsis thaliana lacO/LacI-GFP lines used in this study are in the CoI-0 background. Seeds of the lines #26 and #112 were sterilized for 5 min in 70% ethanol and dried before sowing on 100x15 mm Petri dishes containing 1x MS media supplemented with 1% sucrose, vitamins (1 μg/ml thiamine, 0.5 μg/ml pyridoxine and 0.5 μg/ml nicotinic acid), 0.05% MES and 0.8% agar. The pH of the media was adjusted to 5.5. Seeds were stratified in the dark at 4°C for 2-3 days to synchronize germination and grown vertically under continuous light (150 µmol photons m⁻² s⁻¹). 5-day-old seedlings were transferred onto new MS plates containing 0 (control) or 10 µM B02 for 16-18h. For measurements, the seedlings were placed in 35 mm glass-bottom dishes (MatTek) and covered with media 'slabs' with the same composition as described above. Image sequences were recorded from the root division zone at 40x magnification, with the same IX83 microscope used for mammalian Lac arrays (see above). The temperature was maintained at 22°C by cooling the room to approx. 18°C and heating the custom microscope enclosure to the desired temperature. The acquisition time was 15 min, with 6 sec intervals. Z-stacks were collected over a 3 µm range (7 frames, 0.5 µm z-spacing). Focus was maintained with a laser-based z-drift compensation system (TruFocus; IX3-ZDC). Image pre-processing was done in FIJI. Maximal intensity projections were generated from the z-stacks and intensity was normalized throughout time series. Images (corresponding to the entire root division zone) were registered using StackReg and LacI-GFP spots tracked with the MOSAIC 2D tracker. For paired particle tracking, individual cells were cropped from the movies before tracking. The distance between the two spots, retrieved from the x/y spot coordinates was used to generate MSD using custom code in MATLAB.

Single nucleosome tracking

We used U2OS cells stably expressing H2B fused to the HaloTag and a custom-built oblique light sheet microscope for single nucleosome tracking, as described (Kefer *et al.*, 2021). Before imaging, the cells were incubated with 10 pM fluorescent JF 646 HaloTag ligand (Grimm *et al.*, 2015) for 1h, washed with PBS, and incubated in DMEM without phenol red for at least 30 min. Cells were kept at 37°C in a live cell imaging chamber (Tokai Hit). Images were taken with a 60x oil immersion objective (N.A. = 1.2, Olympus, also used to generate the oblique light sheet), an ORCA-Flash 4.0 sCMOS camera, and a solid-state 640 nm laser. μ Manager (Edelstein *et al.*, 2014) was used to capture images at a frame rate of 20 fps. Single nucleosome motions were quantified with custom software written in Python. Briefly, the localization of each nucleosome spot was detected and fitted with a two-dimensional Gaussian function. Nucleosomes trajectories

were established with a multitemporal association tracking algorithm and used to compute MSD from which the diffusion coefficient *D* was calculated.

Super-resolution imaging of single nucleosomes

The same imaging platform as for single nucleosome tracking was used for dSTORM. Cells were labelled (1pM, 16 hrs), washed and fixed in 3.7% folmaldehyde solution in PBS buffer (pH = 7.5). Prior to imaging, dSTORM buffer was added to the cells. This buffer is based on glucose oxidase / catalase / cysteamine, as described (Van de Linde *et al.*, 2011). Images were acquired at a rate of 100 fps using μ Manager with a laser power of 20 mW at the objective. For single nucleosome localization, we first selected nuclear regions and reduced background noise using FIJI's rolling ball method with a radius of 10 pixels. To minimize the localization error caused by pixel dependent readout noise from sCMOS cameras, we used an iterative algorithm (Huang *et al.*, 2013) that uses a maximum likelihood estimation of the position and intensity of each nucleosome (Smith *et al.*, 2010). After obtaining precise x, y positions of each nucleosome, we analyzed the clustering using Besag's L-function L(r) (Besag, 1977). The L-function (Equation 1) is obtained by transforming Ripley's K-function K(r) in Equation 2 where a is the area of the window, r is the distance separation, and n is the number of data points (Ripley, 1977). The indicator function $I(d_{ij} \le r)$ gives 1 if the distance is less than or equal to r. Degree of clustering is measured by L(r) - r.

$$K(r)=rac{a}{n(n-1)} \sum_{ij} Iig(d_{ij} \le rig)$$
 Equation 1
$$L(r)=\sqrt{rac{K(r)}{\pi}}$$

Immunofluorescence

Immunofluorescence analyses of fixed U2OS cells was done as described previously (Locatelli *et al.*, 2022), with antibodies against RAD51 (AbCam, cat# Ab63801; 1:300), γ H2AX (Millipore, clone JBW301, 2 μ g/ml); H3K9me3 (Cell Signaling, cat# 13969S; 1:800), and H2K9ac (AbCam, cat# Ab12179; 1:500). Secondary antibodies were coupled to AlexaFluor dyes (Life Technologies; 1:500). Nuclei were stained with 0.5 μ g/ml 4',6-diamidino-2-phenylindole (DAPI). Samples were mounted using ProLong Gold antifade (Molecular probes) and imaged with an IX83 Olympus microscope, using a 60x oil immersion objective (N.A. = 1.35) and the appropriate filter cubes (Chroma).

Imaging cytometry

To assess cell cycle distribution, DAPI-stained nuclei were imaged with a 4x (N.A. = 0.13) lens and a qCMOS camera (ORCA-Quest, Hamamatsu) on an IX83 fluorescence microscope, applying shading correction. Background was subtracted using FIJI's built-in rolling ball method (using a radius of 100 pixels). Nuclei were segmented with StarDist (Schmidt *et al.*, 2018) to retrieve integrated densities of DAPI signals. Since signal intensity varied slightly between images, intensity values for each nucleus of an image were scaled by subtracting the mode value (corresponding to the G1 peak position), then adding an arbitrary value (400) to avoid negative intensities. Intensity histograms were plotted in GraphPad Prism for visualization.

Western blot

Cells were lysed in PBS containing 2% SDS, then sonicated. Protein concentration was quantified using the DC protein assay (BioRad, cat#500-0122), and 30 µg of each sample were resolved by SDS-PAGE. Proteins were transferred onto nitrocellulose membranes for immunoblotting with antibodies against H3K9me3 (Cell Signaling, cat# 13969S; 1:1000), H3K9ac (AbCam, cat# Ab12179; 1:1000), H2A (Cell Signaling, cat# 12349S; 1:1000), RAD51 (AbCam, cat# Ab63801; 1:1000), and HSC70 (SantaCruz, Cat# sc7298; 1:1000). Secondary antibodies were anti-rabbit or anti-mouse horseradish peroxidase-coupled IgGs (GE Healthcare, cat# NA934 and NA931; 1:10000). Enhanced chemiluminescence signals were captured with a Fusion Solo imaging system (Vilber Lourmat) and quantified using FIJI.

Cell viability assay

Cells were seeded in 96-well plates at a density of 10000 cells per well and treated for B02. 10 µl of MTT reagent (3-4,5-dimethylthiazol 2,5-diphenyltetrazolium bromide; 5 mg/ml) were added to each well and incubated in the cell culture incubator for 2 hours. The medium was discarded, and formazan crystals were resuspended in 100 µl DMSO. Absorbance was measured using a microplate reader (Tecan Group, Ltd.) at 650 nm. For clonogenic survival assays, cells were trypsinized and seeded into 12-well plates (10,000 cells/well). Colony formation was visualized after seven days by fixing cells in formalin and staining 20 minutes with crystal violet (0.5% in 20% ethanol). Plates were air-dried before imaging.

Chromatin polymer model

Chromosomes were modeled as bead-spring chains, where each chain is analogous to one of the 32 chromosome arms in budding yeast (Hult *et al.*, 2017). In this model, individual beads represent non-overlapping chromatin segments 5 kb in length. The entire yeast genome is represented by 2803 beads organized across 32 chains (16 chromosomes). Each bead is

described by its x/y/z coordinates and a set of global parameters dictating bead volume, Brownian motion, tensile forces between adjacent beads, viscosity, drag, and interactions with the nuclear membrane (Hult et al., 2017). The 3D coordinates of individuals beads were recomputed every 0.001 seconds of simulation time based on the sum of these forces, generating sequential snapshots of chromatin spatial conformations. The Initial configuration of chromosomes was with centromeres tethered to the inner surface of the nucleus, at the same point, according to the Rabl configuration (Berger et al., 2008; Taddei and Gasser, 2012). The telomeres on each of the arms were also tethered to the inner nuclear membrane across 6 distinct positions. In the starting configuration (time 0), the beads in each arm are arranged linearly between the two tether sites. Crosslinks were coded as the property of select beads to form crosslinks with every other bead that shares this property independent of their chain of origin. Crosslinks are realized as additional springs connecting the centers of two beads and influencing bead positions as additional sources of force. Analogous to springs of the bead-spring model, the crosslinks do not have volume or shape in themselves. When two beads are crosslinked, there is an additional tension force between them of magnitude 50x relative to springs linking the polymer chain. Beads form crosslinks with a bead that is not currently crosslinked to another bead; every pair of crosslinked beads will remain bound for a set amount of time or until the distance between them exceeds 90 nm. Once a crosslinker detaches, both beads are unavailable for crosslinking for a set amount of time. The ratio of bound-to-unbound time is defined in initial parameters of the simulation as the Mean On / Off time (Walker et al., 2019). To allow the system to normalize, data collection began after 2400 seconds of simulation time. The 3D coordinates of individual beads were saved every dT = 0.1 s, for a total of 1300 s of data per simulation. The simulation code, code to generate MSD, and the exponential function fit were run in ImageTank (Visual Data Tools).

Statistical analyses

Statistical analyses were done using GraphPad Prism 9. The D'Agostino & Pearson omnibus normality test was used to verify normal distributions. Nonparametric tests were used if the data did not pass the normality test (at alpha = 0.05). The t-test (or Mann-Whitney test) was used for comparisons between two conditions, whereas ANOVA and Tukey post-hoc test (or Kruskal-Wallis and Dunn's multiple comparisons test) was used for datasets with more than two conditions. P-values < 0.05 were considered significant. All statistical tests were two-sided. The box and whisker plots represent medians, 25-75th percentiles (boxes), and 10-90th percentiles (whiskers).

ACKNOWLEDGEMENTS

We thank Dr. Stefanie Rosa for providing the *lacO/*LacI-GFP Arabidopsis lines, and Cloé Dehours and Arnaud Quentel for technical assistance. We are grateful to Dr. George Holzwarth for his contribution in developing MATLAB code, and for productive discussions. This work was funded by the National Cancer Institute (U01CA214282 to P.-A. Vidi and K. Bonin), the National Institute of General Medical Sciences (NIH R01GM32238-37 to K. Bloom and NIH 1R35GM147412 to J. Liu), the National Science Foundation (NSF 2239262 to J. Liu), and by institutional funds from the Institut de Cancérologie de l'Ouest.

REFERENCES

Aymard, F., Bugler, B., Schmidt, C.K., Guillou, E., Caron, P., Briois, S., Iacovoni, J.S., Daburon, V., Miller, K.M., Jackson, S.P., and Legube, G. (2014). Transcriptionally active chromatin recruits homologous recombination at DNA double-strand breaks. Nat Struct Mol Biol *21*, 366-374.

Bancaud, A., Huet, S., Daigle, N., Mozziconacci, J., Beaudouin, J., and Ellenberg, J. (2009). Molecular crowding affects diffusion and binding of nuclear proteins in heterochromatin and reveals the fractal organization of chromatin. The EMBO journal *28*, 3785-3798.

Benson, F.E., Stasiak, A., and West, S.C. (1994). Purification and characterization of the human Rad51 protein, an analogue of E. coli RecA. The EMBO journal *13*, 5764-5771.

Berger, A.B., Cabal, G.G., Fabre, E., Duong, T., Buc, H., Nehrbass, U., Olivo-Marin, J.C., Gadal, O., and Zimmer, C. (2008). High-resolution statistical mapping reveals gene territories in live yeast. Nat Methods *5*, 1031-1037.

Besag, J. (1977). Comments on Ripley's paper: Royal Statistical Society. Journal 39, 193-195.

Bonin, K., Smelser, A., Moreno, N.S., Holzwarth, G., Wang, K., Levy, P., and Vidi, P.A. (2018). Structured illumination to spatially map chromatin motions. J Biomed Opt 23, 1-8.

Budke, B., Logan, H.L., Kalin, J.H., Zelivianskaia, A.S., Cameron McGuire, W., Miller, L.L., Stark, J.M., Kozikowski, A.P., Bishop, D.K., and Connell, P.P. (2012). RI-1: a chemical inhibitor of RAD51 that disrupts homologous recombination in human cells. Nucleic acids research *40*, 7347-7357.

Challa, K., Schmid, C.D., Kitagawa, S., Cheblal, A., Iesmantavicius, V., Seeber, A., Amitai, A., Seebacher, J., Hauer, M.H., Shimada, K., and Gasser, S.M. (2021). Damage-induced chromatome dynamics link Ubiquitin ligase and proteasome recruitment to histone loss and efficient DNA repair. Molecular cell *81*, 811-829 e816.

Cho, N.W., Dilley, R.L., Lampson, M.A., and Greenberg, R.A. (2014). Interchromosomal homology searches drive directional ALT telomere movement and synapsis. Cell *159*, 108-121.

Crossley, M.P., Bocek, M., and Cimprich, K.A. (2019). R-Loops as Cellular Regulators and Genomic Threats. Molecular cell 73. 398-411.

Dimitrova, N., Chen, Y.C., Spector, D.L., and de Lange, T. (2008). 53BP1 promotes non-homologous end joining of telomeres by increasing chromatin mobility. Nature *456*, 524-528.

Dion, V., Kalck, V., Seeber, A., Schleker, T., and Gasser, S.M. (2013). Cohesin and the nucleolus constrain the mobility of spontaneous repair foci. EMBO reports *14*, 984-991.

Edelstein, A.D., Tsuchida, M.A., Amodaj, N., Pinkard, H., Vale, R.D., and Stuurman, N. (2014). Advanced methods of microscope control using µManager software. Journal of biological methods 1.

Feretzaki, M., Pospisilova, M., Valador Fernandes, R., Lunardi, T., Krejci, L., and Lingner, J. (2020). RAD51-dependent recruitment of TERRA IncRNA to telomeres through R-loops. Nature *587*, 303-308.

Garcia Fernandez, F., Almayrac, E., Carre Simon, A., Batrin, R., Khalil, Y., Boissac, M., and Fabre, E. (2022). Global chromatin mobility induced by a DSB is dictated by chromosomal conformation and defines the HR outcome. eLife *11*.

Garcia Fernandez, F., and Fabre, E. (2022). The Dynamic Behavior of Chromatin in Response to DNA Double-Strand Breaks. Genes (Basel) 13.

Girasol, M.J., Krasilnikova, M., Marques, C.A., Damasceno, J.D., Lapsley, C., Lemgruber, L., Burchmore, R., Beraldi, D., Carruthers, R., Briggs, E.M., and McCulloch, R. (2023). RAD51-mediated R-loop formation acts to repair transcription-associated DNA breaks driving antigenic variation in Trypanosoma brucei. Proceedings of the National Academy of Sciences of the United States of America *120*, e2309306120.

Grimm, J.B., English, B.P., Chen, J., Slaughter, J.P., Zhang, Z., Revyakin, A., Patel, R., Macklin, J.J., Normanno, D., Singer, R.H., Lionnet, T., and Lavis, L.D. (2015). A general method to improve fluorophores for live-cell and single-molecule microscopy. Nat Methods *12*, 244-250, 243 p following 250.

Gu, B., Swigut, T., Spencley, A., Bauer, M.R., Chung, M., Meyer, T., and Wysocka, J. (2018). Transcription-coupled changes in nuclear mobility of mammalian cis-regulatory elements. Science *359*, 1050-1055.

Halder, S., Sanchez, A., Ranjha, L., Reginato, G., Ceppi, I., Acharya, A., Anand, R., and Cejka, P. (2022). Double-stranded DNA binding function of RAD51 in DNA protection and its regulation by BRCA2. Molecular cell *82*, 3553-3565 e3555.

Harper, J.V. (2005). Synchronization of cell populations in G1/S and G2/M phases of the cell cycle. Methods in molecular biology 296, 157-166.

Hazan, I., Monin, J., Bouwman, B.A.M., Crosetto, N., and Aqeilan, R.I. (2019). Activation of Oncogenic Super-Enhancers Is Coupled with DNA Repair by RAD51. Cell reports 29, 560-572 e564.

Herbert, S., Brion, A., Arbona, J.M., Lelek, M., Veillet, A., Lelandais, B., Parmar, J., Fernandez, F.G., Almayrac, E., Khalil, Y., Birgy, E., Fabre, E., and Zimmer, C. (2017). Chromatin stiffening underlies enhanced locus mobility after DNA damage in budding yeast. The EMBO journal *36*, 2595-2608.

- Heun, P., Laroche, T., Shimada, K., Furrer, P., and Gasser, S.M. (2001). Chromosome dynamics in the yeast interphase nucleus. Science *294*, 2181-2186.
- Huang, F., Hartwich, T.M., Rivera-Molina, F.E., Lin, Y., Duim, W.C., Long, J.J., Uchil, P.D., Myers, J.R., Baird, M.A., and Mothes, W. (2013). Video-rate nanoscopy using sCMOS camera—specific single-molecule localization algorithms. Nature methods *10*, 653-658.
- Huang, F., Mazina, O.M., Zentner, I.J., Cocklin, S., and Mazin, A.V. (2012). Inhibition of homologous recombination in human cells by targeting RAD51 recombinase. J Med Chem *55*, 3011-3020.
- Huang, F., Motlekar, N.A., Burgwin, C.M., Napper, A.D., Diamond, S.L., and Mazin, A.V. (2011). Identification of specific inhibitors of human RAD51 recombinase using high-throughput screening. ACS Chem Biol *6*, 628-635.
- Hult, C., Adalsteinsson, D., Vasquez, P.A., Lawrimore, J., Bennett, M., York, A., Cook, D., Yeh, E., Forest, M.G., and Bloom, K. (2017). Enrichment of dynamic chromosomal crosslinks drive phase separation of the nucleolus. Nucleic acids research *45*, 11159-11173.
- lida, S., Shinkai, S., Itoh, Y., Tamura, S., Kanemaki, M.T., Onami, S., and Maeshima, K. (2022). Single-nucleosome imaging reveals steady-state motion of interphase chromatin in living human cells. Sci Adv 8, eabn5626.
- Kang, K., Choi, Y., Moon, H., You, C., Seo, M., Kwon, G., Yun, J., Beck, B., and Kang, K. (2021). Epigenomic Analysis of RAD51 ChIP-seq Data Reveals cis-regulatory Elements Associated with Autophagy in Cancer Cell Lines. Cancers (Basel) *13*.
- Kefer, P., Iqbal, F., Locatelli, M., Lawrimore, J., Zhang, M., Bloom, K., Bonin, K., Vidi, P.A., and Liu, J. (2021). Performance of deep learning restoration methods for the extraction of particle dynamics in noisy microscopy image sequences. Mol Biol Cell 32, 903-914.
- Kramarz, K., Schirmeisen, K., Boucherit, V., Ait Saada, A., Lovo, C., Palancade, B., Freudenreich, C., and Lambert, S.A.E. (2020). The nuclear pore primes recombination-dependent DNA synthesis at arrested forks by promoting SUMO removal. Nature communications *11*, 5643.
- Krawczyk, P.M., Borovski, T., Stap, J., Cijsouw, T., ten Cate, R., Medema, J.P., Kanaar, R., Franken, N.A., and Aten, J.A. (2012). Chromatin mobility is increased at sites of DNA double-strand breaks. Journal of cell science *125*, 2127-2133.
- Lawrimore, C.J., Lawrimore, J., He, Y., Chavez, S., and Bloom, K. (2020). Polymer perspective of genome mobilization. Mutat Res *821*, 111706.
- Lawrimore, J., Barry, T.M., Barry, R.M., York, A.C., Friedman, B., Cook, D.M., Akialis, K., Tyler, J., Vasquez, P., Yeh, E., and Bloom, K. (2017). Microtubule dynamics drive enhanced chromatin motion and mobilize telomeres in response to DNA damage. Mol Biol Cell 28, 1701-1711.
- Lisby, M., Rothstein, R., and Mortensen, U.H. (2001). Rad52 forms DNA repair and recombination centers during S phase. Proceedings of the National Academy of Sciences of the United States of America 98, 8276-8282.

Liu, J., Vidi, P.A., Lelievre, S.A., and Irudayaraj, J.M. (2015). Nanoscale histone localization in live cells reveals reduced chromatin mobility in response to DNA damage. Journal of cell science *128*, 599-604.

Locatelli, M., Lawrimore, J., Lin, H., Sanaullah, S., Seitz, C., Segall, D., Kefer, P., Salvador Moreno, N., Lietz, B., Anderson, R., Holmes, J., Yuan, C., Holzwarth, G., Bloom, K.S., Liu, J., Bonin, K., and Vidi, P.A. (2022). DNA damage reduces heterogeneity and coherence of chromatin motions. Proc Natl Acad Sci U S A *119*, e2205166119.

Ma, H., Tu, L.C., Chung, Y.C., Naseri, A., Grunwald, D., Zhang, S., and Pederson, T. (2019). Cell cycleand genomic distance-dependent dynamics of a discrete chromosomal region. The Journal of cell biology 218, 1467-1477.

Meschichi, A., Zhao, L., Reeck, S., White, C., Da Ines, O., Sicard, A., Pontvianne, F., and Rosa, S. (2022). The plant-specific DDR factor SOG1 increases chromatin mobility in response to DNA damage. EMBO reports 23, e54736.

Mine-Hattab, J., and Chiolo, I. (2020). Complex Chromatin Motions for DNA Repair. Frontiers in genetics 11, 800.

Mine-Hattab, J., Recamier, V., Izeddin, I., Rothstein, R., and Darzacq, X. (2017). Multi-scale tracking reveals scale-dependent chromatin dynamics after DNA damage. Mol Biol Cell.

Mine-Hattab, J., and Rothstein, R. (2012). Increased chromosome mobility facilitates homology search during recombination. Nature cell biology *14*, 510-517.

Miron, E., Oldenkamp, R., Brown, J.M., Pinto, D.M.S., Xu, C.S., Faria, A.R., Shaban, H.A., Rhodes, J.D.P., Innocent, C., de Ornellas, S., Hess, H.F., Buckle, V., and Schermelleh, L. (2020). Chromatin arranges in chains of mesoscale domains with nanoscale functional topography independent of cohesin. Sci Adv 6.

Nagashima, R., Hibino, K., Ashwin, S.S., Babokhov, M., Fujishiro, S., Imai, R., Nozaki, T., Tamura, S., Tani, T., Kimura, H., Shribak, M., Kanemaki, M.T., Sasai, M., and Maeshima, K. (2019). Single nucleosome imaging reveals loose genome chromatin networks via active RNA polymerase II. The Journal of cell biology *218*, 1511-1530.

Neumann, F.R., Dion, V., Gehlen, L.R., Tsai-Pflugfelder, M., Schmid, R., Taddei, A., and Gasser, S.M. (2012). Targeted INO80 enhances subnuclear chromatin movement and ectopic homologous recombination. Genes & development 26, 369-383.

Niehrs, C., and Luke, B. (2020). Regulatory R-loops as facilitators of gene expression and genome stability. Nature reviews. Molecular cell biology *21*, 167-178.

Nozaki, T., Imai, R., Tanbo, M., Nagashima, R., Tamura, S., Tani, T., Joti, Y., Tomita, M., Hibino, K., Kanemaki, M.T., Wendt, K.S., Okada, Y., Nagai, T., and Maeshima, K. (2017). Dynamic Organization of Chromatin Domains Revealed by Super-Resolution Live-Cell Imaging. Molecular cell *67*, 282-293 e287.

Oshidari, R., Strecker, J., Chung, D.K.C., Abraham, K.J., Chan, J.N.Y., Damaren, C.J., and Mekhail, K. (2018). Nuclear microtubule filaments mediate non-linear directional motion of chromatin and promote DNA repair. Nature communications *9*, 2567.

Ricci, M.A., Manzo, C., Garcia-Parajo, M.F., Lakadamyali, M., and Cosma, M.P. (2015). Chromatin fibers are formed by heterogeneous groups of nucleosomes in vivo. Cell *160*, 1145-1158.

Ripley, B.D. (1977). Modelling spatial patterns. Journal of the Royal Statistical Society: Series B (Methodological) 39, 172-192.

Sbalzarini, I.F., and Koumoutsakos, P. (2005). Feature point tracking and trajectory analysis for video imaging in cell biology. J Struct Biol *151*, 182-195.

Schmidt, U., Weigert, M., Broaddus, C., and Myers, G. (2018). Cell Detection with Star-Convex Polygons. Medical Image Computing and Computer Assisted Intervention – MICCAI 2018, Cham, 265-273.

Seeber, A., Dion, V., and Gasser, S.M. (2013). Checkpoint kinases and the INO80 nucleosome remodeling complex enhance global chromatin mobility in response to DNA damage. Genes & development 27, 1999-2008.

Seeber, A., Hauer, M.H., and Gasser, S.M. (2018). Chromosome Dynamics in Response to DNA Damage. Annu Rev Genet *52*, 295-319.

Shkundina, I.S., Gall, A.A., Dick, A., Cocklin, S., and Mazin, A.V. (2021). New RAD51 Inhibitors to Target Homologous Recombination in Human Cells. Genes (Basel) *12*.

Smith, C.S., Joseph, N., Rieger, B., and Lidke, K.A. (2010). Fast, single-molecule localization that achieves theoretically minimum uncertainty. Nature methods 7, 373-375.

Smith, M.J., Bryant, E.E., Joseph, F.J., and Rothstein, R. (2019). DNA damage triggers increased mobility of chromosomes in G1-phase cells. Mol Biol Cell *30*, 2620-2625.

Smith, M.J., Bryant, E.E., and Rothstein, R. (2018). Increased chromosomal mobility after DNA damage is controlled by interactions between the recombination machinery and the checkpoint. Genes & development 32, 1242-1251.

Su, X.A., Dion, V., Gasser, S.M., and Freudenreich, C.H. (2015). Regulation of recombination at yeast nuclear pores controls repair and triplet repeat stability. Genes & development 29, 1006-1017.

Taddei, A., and Gasser, S.M. (2012). Structure and function in the budding yeast nucleus. Genetics 192, 107-129.

Thevenaz, P., Ruttimann, U.E., and Unser, M. (1998). A pyramid approach to subpixel registration based on intensity. IEEE Trans Image Process *7*, 27-41.

Tsuzuki, T., Fujii, Y., Sakumi, K., Tominaga, Y., Nakao, K., Sekiguchi, M., Matsushiro, A., Yoshimura, Y., and MoritaT. (1996). Targeted disruption of the Rad51 gene leads to lethality in embryonic mice. Proceedings of the National Academy of Sciences of the United States of America *93*, 6236-6240.

Urban, V., Dobrovolna, J., Huhn, D., Fryzelkova, J., Bartek, J., and Janscak, P. (2016). RECQ5 helicase promotes resolution of conflicts between replication and transcription in human cells. The Journal of cell biology *214*, 401-415.

Van de Linde, S., Löschberger, A., Klein, T., Heidbreder, M., Wolter, S., Heilemann, M., and Sauer, M. (2011). Direct stochastic optical reconstruction microscopy with standard fluorescent probes. Nature protocols *6*, 991-1009.

Vidi, P.A., Chandramouly, G., Gray, M., Wang, L., Liu, E., Kim, J.J., Roukos, V., Bissell, M.J., Moghe, P.V., and Lelievre, S.A. (2012). Interconnected contribution of tissue morphogenesis and the nuclear protein NuMA to the DNA damage response. J Cell Sci *125*, 350-361.

Vydyam, P., Dutta, D., Sutram, N., Bhattacharyya, S., and Bhattacharyya, M.K. (2019). A small-molecule inhibitor of the DNA recombinase Rad51 from Plasmodium falciparum synergizes with the antimalarial drugs artemisinin and chloroquine. J Biol Chem *294*, 8171-8183.

Wahba, L., Gore, S.K., and Koshland, D. (2013). The homologous recombination machinery modulates the formation of RNA-DNA hybrids and associated chromosome instability. eLife 2, e00505.

Walker, B., Taylor, D., Lawrimore, J., Hult, C., Adalsteinsson, D., Bloom, K., and Forest, M.G. (2019). Transient crosslinking kinetics optimize gene cluster interactions. PLoS Comput Biol *15*, e1007124.

Wassing, I.E., and Esashi, F. (2021). RAD51: Beyond the break. Semin Cell Dev Biol 113, 38-46.

Zaitseva, E.M., Zaitsev, E.N., and Kowalczykowski, S.C. (1999). The DNA binding properties of Saccharomyces cerevisiae Rad51 protein. J Biol Chem 274, 2907-2915.

Zhang, H., Shi, Z., Banigan, E.J., Kim, Y., Yu, H., Bai, X.C., and Finkelstein, I.J. (2023). CTCF and R-loops are boundaries of cohesin-mediated DNA looping. Molecular cell *83*, 2856-2871 e2858.

FIGURES AND LEGENDS

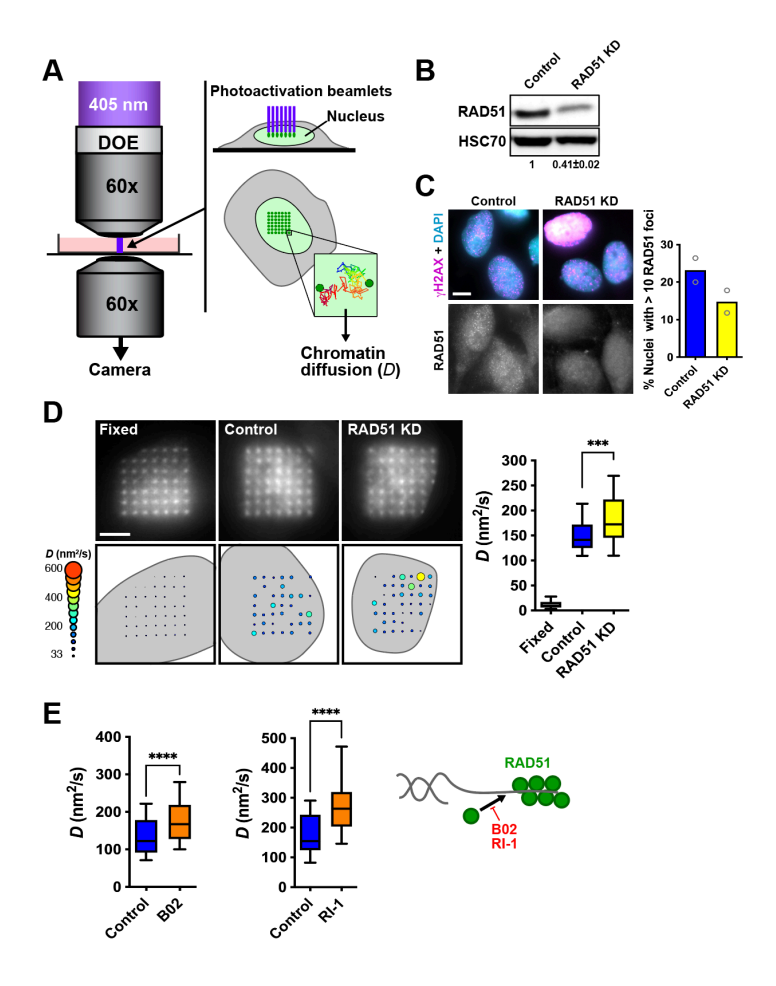


Figure 1. RAD51 regulates chromatin motions at the microscale. **A** Schematic illustration of the structured illumination system used to track chromatin microdomain motions in cells expressing PAGFP-H2A. **B-C** Knock-down (KD) of RAD51 expression in U2OS cells verified by western blot (**B**) and immunostaining (**C**). Immunoblot signal intensities were quantified by densitometry. Normalized intensity values are shown below the blots (mean \pm SD; N = 2). Cells used for immuostaining were treated with MMC to induce DNA damage. The proportion of nuclei that accumulated RAD51 foci is shown in the graph (N = 2). Scale bar, 10 μm. **D** Representative images of the photoactivated chromatin lattices (PAGFP-H2A) and corresponding diffusion (*D*) values (bubble plots) in control and RAD51 KD cells. Measurements with fixed cells show a modest contribution of noise. Scale bar, 5 μm. *D* values are quantified graph. ***, P = 0.0005 (Mann Whitney test). N = 50-90 cells from 3 independent experiments. **E** Chromatin microdomain diffusion in cells treated with RAD51 inhibitors B02 (100 μM) and RI-1 (25 μM). ****, P < 0.0001 (t-test). N = 30 - 100 cells from 2 biological replicates.

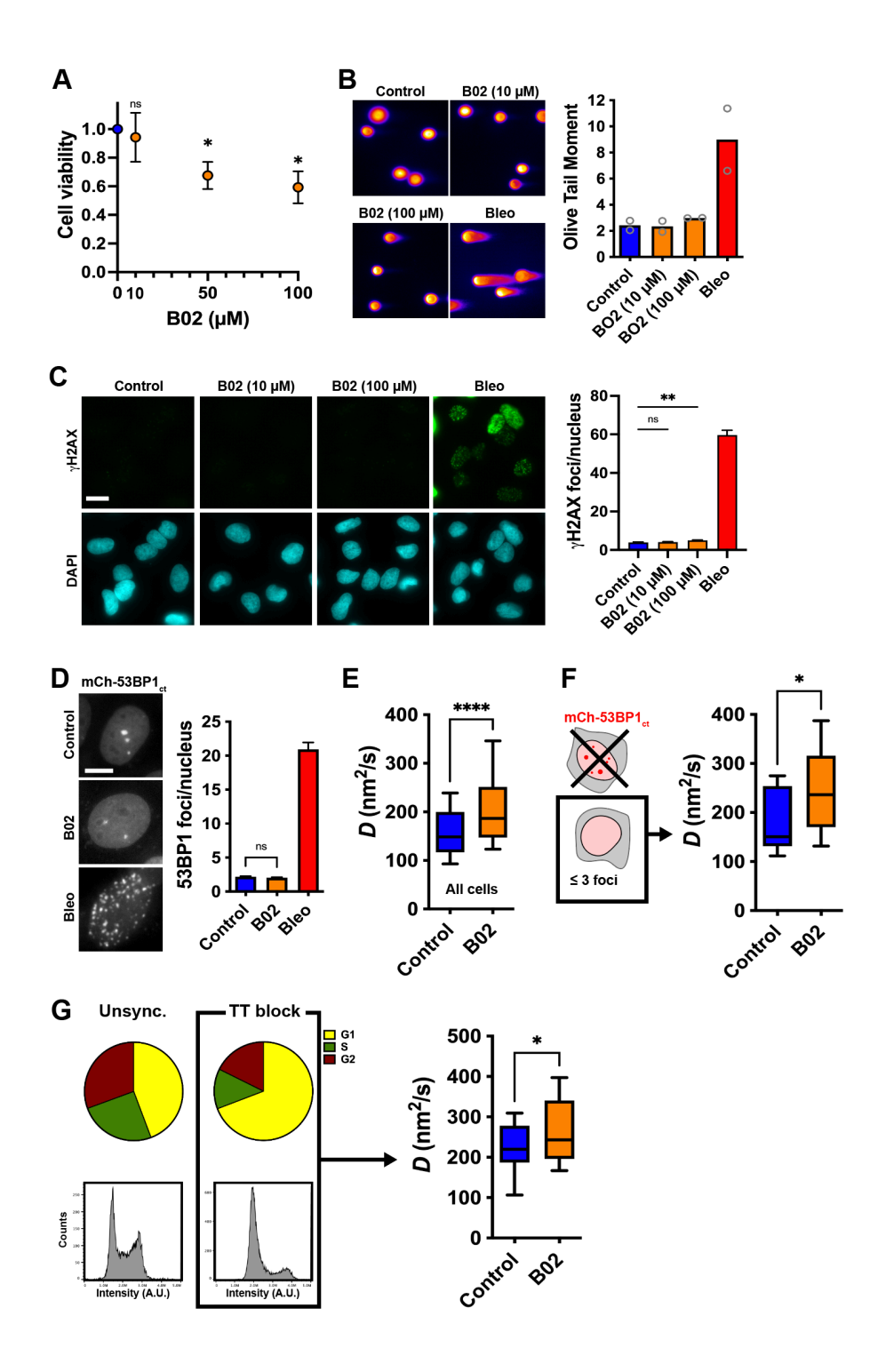


Figure 2. Increased chromatin microdomain mobility upon RAD51 inhibition is independent from DNA damage. **A** Cell viability, assessed by MTT assay 24h after B02 treatment. Values are normalized to untreated cells. *, P < 0.05; ns, not significant (one-sample t-test; N = 3 biological

replicates). B Detection of DNA double-strand breaks with neutral comet assays in cells treated with B02 (10 or 100 µM, 1h). Bleomycin treatment (Bleo; 20 mU/ml for 1h) was used as positive control. Averaged values from two biological replicates (>300 cells/condition) are shown in the graph. C γH2AX immunostaining of cells treated as in (B). Scale bar, 10 μm. γH2AX foci quantification is shown in the graph. **, P < 0.01; ns, not significant (Kruskal-Wallis and Dunn's multiple comparisons test; N > 300 cells from two biological replicates). D DNA break foci (labeled with mCherry-53BP1ct) in cells treated with B02 (10 µM, 1h). Gamma adjustment (0.5) was performed to visualize both nucleoplasmic signals and DSB foci. Scale bar, 10 µm. DSB foci are quantified in the bar graph (mean ± SEM). ns, not significant; N = 900-1000 cells from 3 independent experiments. E Chromatin diffusion (D) in untreated U2OS cell and in cells treated with B02 (10 μ m, 1h). ****, P < 0.0001; N = 53 (control) and N = 100 (B02) cells from 3 independent experiments. F Chromatin D values in cells treated as in (E), but only including cells with ≤ 3 mCh-53BP1_{ct} DSB foci, to avoid cells with endogenous DNA breaks. *, P = 0.003; N = 12 (control) and N = 16 (B02) cells from 3 experiments. **G** Effect of B02 on chromatin diffusion in G1 phase. Enrichment of the G1 cell population after synchronization with a double thymidine (TT) block was confirmed by flow cytometry (left). Chromatin D values are shown in the graph. *. P = 0.013: N = 39 (control) and 41 (B02) cells from two experiments.

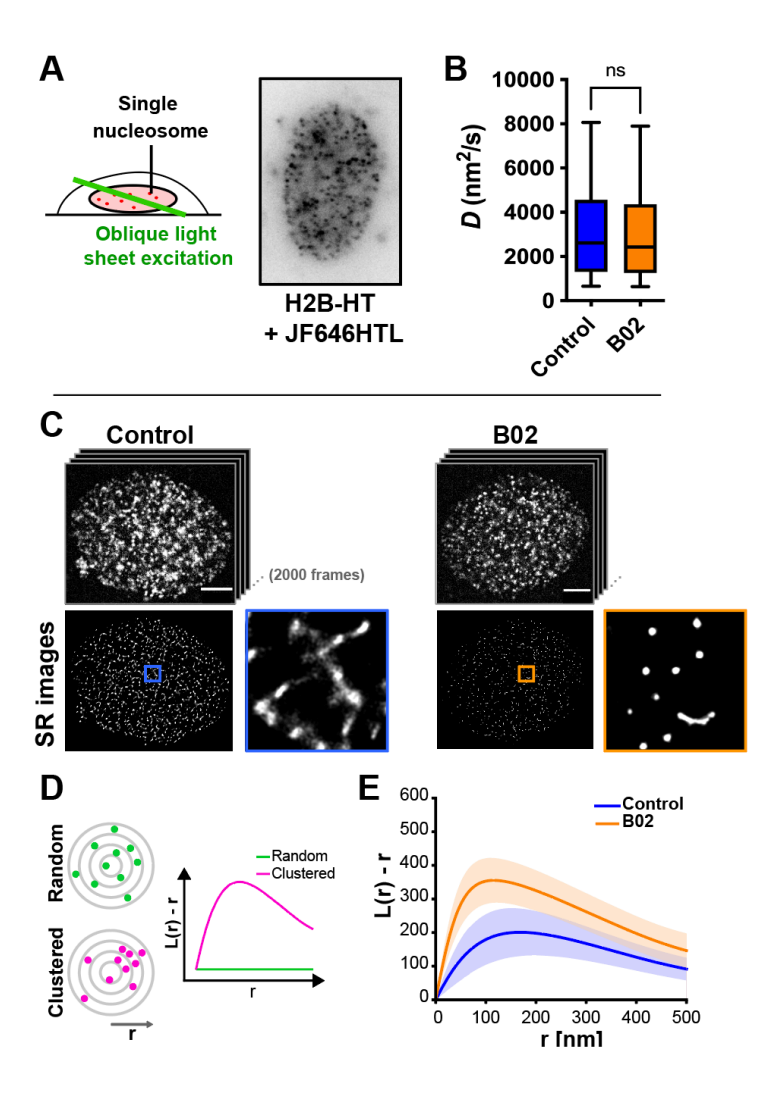


Figure 3. RAD51 inhibition does not impact single nucleosome motions but increases nucleosome clustering. **A** Schematic of oblique light sheet imaging of single nucleosomes and micrograph of a U2OS cell expressing histone 2B fused to HaloTag (H2B-HT) labeled with JF646 HaloTag ligand (HTL). **B** Diffusion of single nucleosomes in untreated cells and in cells treated with B02 (10 μ m, 1h); ns, not significant (P = 0.07; N = 3391 [Control] and N = 3661 [B02] nucleosome traces from two independent experiments). **C** Representative dSTORM superresolution (SR) images of cells treated as in (B). Scale bars, 5 μ m. **D** Illustration of spot cluster analysis using Besag's L-function. A random particle distribution along the radius of the nucleus (r) yields a flat line whereas a peak in the function indicates clustering. The amplitude and position of the peak describes the degree of clustering at a given distance band. **E** Nucleosome cluster analysis of untreated and B02-treated cells. Means \pm SD are shown. N = 12 (control) and N = 18 (B02) cells.

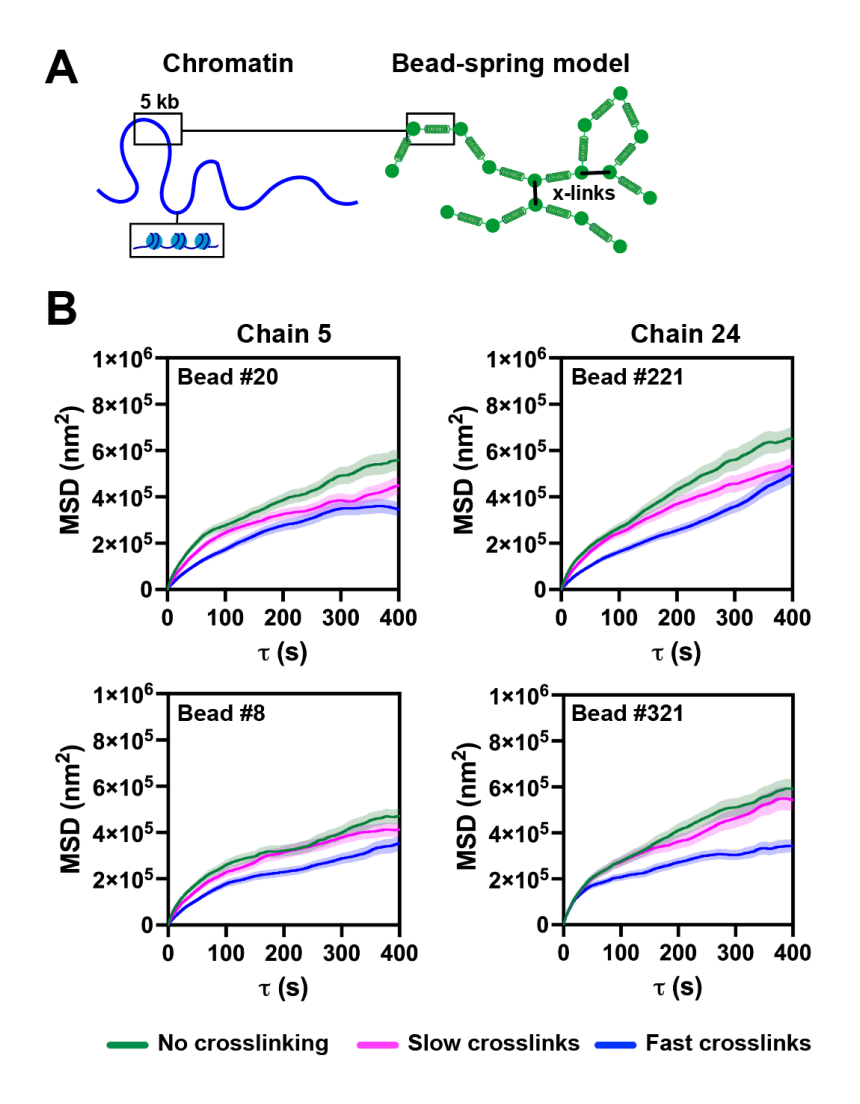


Figure 4. Relationship between chromatin crosslinking and mobility in a polymer model. **A** Schematic illustration of the bead-and-spring chromatin model at 5 kilobase (kb) resolution. **B** Mean square displacement (MSD) plots of beads in the polymer model corresponding to the left arm of chromosome III (Chain 5, 24 beads total) or to the right arm of chromosome XII (Chain 24, 546 beads total). The plots represent mean ± SEM (N = 10 simulations) of different beads. Different looping behaviors were compared: no crosslinking (green), long crosslink lifetimes (slow crosslinking, pink), and short crosslink lifetimes (fast crosslinking, blue).

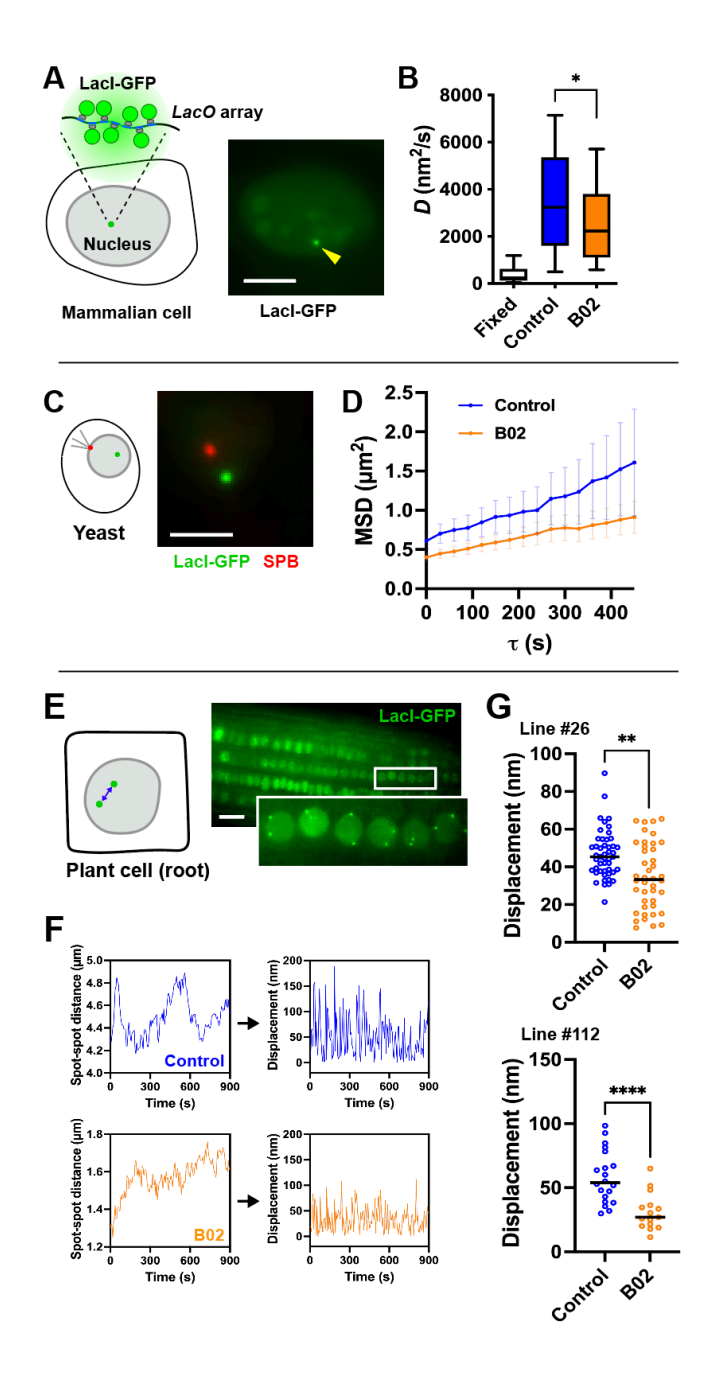


Figure 5. RAD51 inhibition reduces motions of individual chromatin loci across species. **A** Schematic and micrograph of a U2OS cell with a genomic integration of *lacO* DNA arrays and expressing the lac repressor fused to GFP (LacI-GFP). Gamma adjustment (0.5) was performed for visualization of both the LacI-GFP focus and pan-nuclear signals. Scale bar, 10 μ m. **B** Diffusion (*D*) of LacI-GFP foci in untreated cell and in cells treated with B02 (10 μ M, 1h). Fixed cells were used as controls. *, P = 0.042; N = 37 (fixed cells), N = 57 (control), and N = 81 (B02)

LacI-GFP foci from 3 independent experiments. **C** Yeasts with a genomic integration of *lacO* visualized with LacI-GFP. A spindle pole body marker (SPB; Spc29-RFP) is used for image registration. Scale bar, 2 μ m. **D** Diffusion of LacI-GFP foci in yeasts treated with B02 (10 μ M, 1h). The control was untreated. The data are presented as a mean squared displacement (MSD) plot (mean \pm SEM; N = 81 [control] and N = 77 [B02]). **E** *LacO*/LacI-GFP in Arabidopsis roots. A file of cell nuclei is shown enlarged in the inset. Scale bar, 20 μ m. **F** Displacement calculated from the motions of spot pairs, corresponding to the fluctuation of spot-spot distances. **G** Quantification of average LacI-GFP spot displacements. Roots were placed on regular MS medium (control) or on medium supplemented with B02 (10 μ M) for 18h before the measurements. The symbols represent individual cells from two different lines (#26 and #112). **, P = 0.0011; *****, P < 0.0001